Germanium on silicon SPAD 32x32 pixel array in 3D-stacked technology for SWIR applications

Y. Benhammou[1], N. Moussy[2], R. Paquet[2], C. Buj[2], O. Saxod[2],
D. Rideau[3], D. Pellissier-Tanon[3], S. Pellegrini[5], F. Calmon[4], D. Golanski[3]

[1]D&FD, STMicroelectronics, Tours, France,[2]CEA-LETI, Minatec Campus, Grenoble, France,
[3]TR&D, STMicroelectronics, Crolles, France email: dominik.golanski@st.com, [4]INL, Université de Lyon, INSA Lyon, France, [5]Imaging Division, STMicroelectronics, Edinburgh, Scotland

***Abstract*— We present a unique integration of a Single Photon Avalanche Diode (SPAD) silicon matrix with a germanium absorber stacked on a CMOS 40nm technology readout circuit. This architecture extends the sensitivity of the silicon SPAD to the Short-Wave Infrared (SWIR). A careful optimization of the process was performed to reduce the dislocations in the germanium epitaxy. The use of a relatively highly doped germanium combined with small dimension area of the pixels lead to a Dark Count Rate (DCR) level contained below 10 kcps (kilo counts per second) at -40°C and 2V excess bias. The light sensitivity at 1300 nm wavelength is maintained at a reasonable level with a Photo Detection Probability (PDP) of 7 %. These results are obtained with a remarkable low dispersion over several thousands of SPADs. A noise equivalent power of 3E-17 W.Hz$^{-1/2}$ is obtained at 1300 nm wavelength and -40°C.**

Keywords— SPAD, SWIR, LIDAR, Germanium, 3D Integration.

I. INTRODUCTION

3-D mapping at medium range distance have found technical solutions with direct or indirect time of flight using silicon detectors. These active illumination techniques work around 940 nm wavelength compatible with silicon sensitivity. Above few tens of meters, high sensitivity or higher illumination power are required. Eye-safety constraints are relieved by more than a factor 10 by extending the spectral range in the SWIR with the LiDAR solutions [1]. Materials such as Germanium [2] [3] and III-V semiconductors InGaAs/InP SPADs [4] [5] can be considered for that purpose.

A controlled noise level can be achieved by using germanium-based detectors with well-Separated Absorption, Charge and Multiplication regions (SACM). The silicon region is used as the multiplication region with a high field PN junction and the germanium region as the absorber [2] [3]. Vines et al [6], reported a high-performance Germanium-on-PiN Silicon SPAD by reducing the electric field in the germanium.

This work reports a fully integrated 3D-stacked 32x32 pixels embedding Ge on Si SPAD device on a CMOS 40nm technology. Dark currents and sensitivity performances are discussed varying the doping level of germanium, excess voltage and operating temperature.

II. SPAD DEVICE ARCHITECTURE

This device is based on an available architecture for silicon SPAD technology [7] with an additional germanium epitaxy and process adaptations (Fig.1). The top tier wafer hosting the SPAD is bonded on a 40nm CMOS technology 12-inches bottom wafer (Fig.2). Each SPAD has a single connection on a 32x32 readout circuit including passive quenching and pulse counting. The pitch of the matrix is 14.5 µm horizontally and 23.5 µm vertically. The top tier is thinned for contact enabling.

The avalanche junction of the SPAD is formed between the PWELL and the deep NWELL implants. It is surrounded by a guard ring realized with an undoped epitaxial layer (EPI) and a shallow trench isolation (STI) (Fig.1). A square cavity less than 1µm deep and a few µm wide is etched in the active silicon. A germanium island is grown inside the cavity by a selective in-situ-doped epitaxy. This area of the cavity is considered for PDP estimation. A 10.5% fill factor is obtained at the pitch of the matrix.

Boron in-situ doping of the germanium is assessed at two concentrations: a highly doped layer and a lowly doped layer. Surface passivation and top contact of germanium are done with a surface boron implantation. An additional Ring implant with boron aims to inhibit the periphery of the cavity where defects and the shape of the cavity can cause early breakdown effects. The second role of this ring is to prevent the leakage of photogenerated carriers at the periphery of the diode.

III. OPERATING PRINCIPLE

Process and electrical simulations are performed with the Synopsys Sentaurus commercial suite. A cartography of the doping scheme of the device is shown Fig.1. While increasing reverse bias on the PN junction, the depletion region extends through the PWELL, the Ge-Si interface and finally into the germanium. Charges can flow through the device above the Punch-Through polarization (Vpt) when the depletion reaches the Ge-Si interface. The doping profiles and thickness of PWELL are tuned in order to obtain a Breakdown Voltage (BV) close to the polarization Vpt. Excess voltage, variations of PWELL dose and Ge doping modify the electric field entering into the germanium (Fig.3) and permit to explore its incidence on sensitivity and dark current.

Technology computer-aided design (TCAD) simulations were performed with the introduction of defects at the heterojunction and in the germanium bulk at a density level proposed by [8] [9]. As expected, higher germanium doping prevents the expansion of the depletion region and reduces the dark currents. The level of these currents and effect of Ge doping on the collection of photogenerated carrier can only be evaluated experimentally.

IV. CHARACTERIZATION RESULTS

A. Currents on stand alone SPAD

Current behavior strongly depends on the doping level of the PWELL as illustrated in Fig.4 at room temperature. The punch through and the breakdown voltage evolution with the PWELL dose is extracted in Fig.5. Two wafers show the closest Vpt≈18V and BV≈20V. One wafer has a high doped germanium, the second one has low doped germanium.

Fig.6 shows the SPAD current-voltage measurements on two different locations on the wafers. The variation Vpt and BV is attributed to a slow modulation of the thickness of PWELL over the surface. The dark currents above Vpt only differ by a factor of 2 between the two wafers. The current density is approximately 8E-5 A.cm-2 over the surface of the germanium cavity at room temperature.

B. 32x32 SPAD array

The 32x32 readout circuit gives access to the count per second (cps) of each individual pixel. The high voltage (VHV) is common to all SPADs and adjusted for each circuit using the median voltage of avalanche detection of the pixels. In order to suppress residual cross talk, only ¼ of the SPADs are biased at the same time above BV during measurements. SPADs with high count rates are also disabled.

In Fig.7 and 8, the thin dot-line plot displays the median, min and max values statistics of each device with 1024 SPADs. At -40°C, the DCR is limited below 10 kcps and the PDP at 1300 nm wavelength reaches 7% at 2V excess bias. The 1-sigma uniformity of BV is less than 80 mV inside the devices. The evolution of the breakdown voltage in temperature measured at +18mV/°C follows the standard behavior of silicon SPAD. The progression of dark counts with temperature follows an Arrhenius law with an activation energy Ea=0.75 eV close to the gap of germanium.

Fig.9 and 10 show the performances of both the lowly and highly doped germanium. As expected DCR is better with a higher doping and also sensitivity is almost 2 times better. These good results are relatively free of artifacts with less than 1% afterpulses and 7 ns pulse duration up to an excess bias of 2V. The afterpulse rate is measured via a histogram of inter-arrival time of dark count pulses (Fig.11). This very low rate corresponds to silicon behavior. Germanium is probably only weakly involved in this effect.

Around 1% PDP sensitivity is measured at 1550nm due to the natural absorption cutoff of germanium and the thickness used for this demonstration (Fig.12). The absorption at 1300 nm wavelength through 300 nm thick germanium is estimated around 20% and the PDP is measured around 7%. Ignoring the reflections inside the 3D stack, these results show that the internal efficiency of the detector is around 35%. The rest of photogenerated carriers are recombined inside the germanium layer and at the heterojunction, or fail to generate an avalanche.

The sensitivity to light increases with temperature from 7% at -40°C to 11% at 0°C, as observed in Fig.13. The driving contribution to this evolution has not yet been identified, among the possible temperature effects of light absorption [10] [11], impact ionization and heterojunction transfer.

Jitter measured on several SPADs using a 30 ps pulsed laser at 1310 nm wavelength (PicoQuant) shows a diffusion tail that varies little with excess voltage (Fig.14). Full width at half maximum (FWHM) and at 1% of maximum (FWM100) are respectively 140 ps and 1100 ps at 2V excess bias and -40°C (Fig.15). These low jitter values most probably result from the low thickness of the germanium layer.

The Fig.16 shows a comparison of the Noise Equivalent Power (NEP) between several publications including InGaAs SPAD technology [6][12][13][14]. The $\mathrm{NEP} = \mathrm{h}\nu * \frac{\sqrt{2.DCR}}{\mathrm{PDE}}$ is calculated with the Photo Detection Efficiency (PDE) defined over the pitch of the matrix. The very good result on this figure of merit with a remarkable improvement in temperature is obtained thanks to a minimized DCR noise and by a very contained afterpulsing.

Overall pixel performance can be improved by the addition of light sensitivity boosters such as higher Ge layer thickness, improved Fill Factor with smaller readout circuit and improved light collection and confinement by the use of micro-lenses and the engineering of light reflections. DCR can be further reduced with Germanium cavity area reduction and doping optimization.

[1] Dolcera – Self Driving Cars, Sept 2016.

[2] R. Warburton et al, “Ge-on-Si SPAD Modeling and Characterization at 1310 and 1550 nm” IEEE Transactions Electron Devices, Vol. 60, No. 11, November 2013.

[3] Z. Lu et al “Geiger-Mode Operation of Ge-on-Si Avalanche Photodiodes” IEEE J. of Quantum Electronics, Vol.47, No. 5, May 2011.

[4] A. Tosi, A. Dalla Mora, F. Zappa and S. Cova “Germanium and InGaAs/InP SPADs for Single-Photon Detection in the Near-Infrared” Proceedings of SPIE Vol. 6771 67710P-1.

[5] M. Sanzaro et al. “InGaAs/InP Single Photon Avalanche Diode With Monolithically Integrated Zinc-Diffused Resistor” IEEE Journal of Quantum Electronics, Vol. 52, No. 7, July 2016.

[6] P. Vines et al, “High performance planar Germanium-on-silicon SPAD detectors” NATURE COMMUNICATIONS | (2019) 10:1086.

[7] S. Pellegrini et al, “Industrialised SPAD in 40 nm Technology” 2017 IEEE International Electron Devices Meeting, IEDM17-401, CA.

[8] G. Hellings et al, “Electrical TCAD Simulations of a Germanium PMOSFET Technology” IEEE Transactions Electron Devices, Vol. 57, No. 10, October 2010.

[9] Y. Heng Tan, “Al2O3 Interface Engineering of Germanium Epitaxial Layer Grown Directly on Silicon” IEEE Transactions on Electron Devices, Vol. 60, No. 1, January 2013.

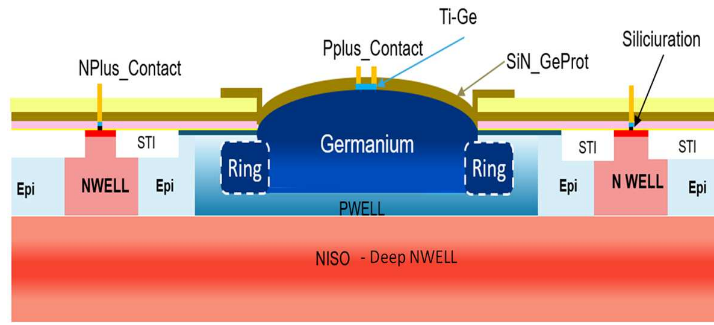

Fig. 1. Architecture of the SPAD with a total dimension of 11.5x11.5 µm²

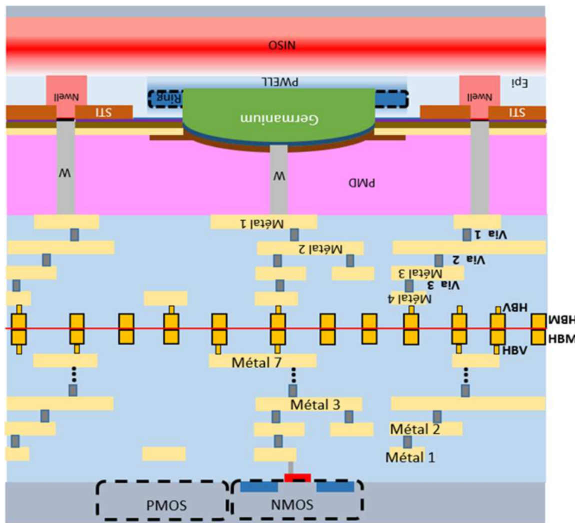

Fig. 2. 3D Integration of the SPAD

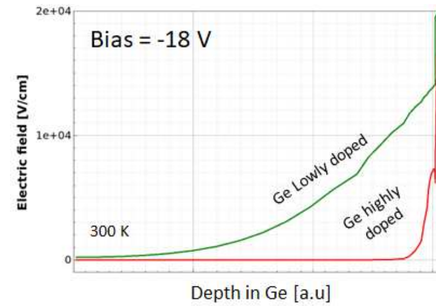

Fig.3 Simulation of electric field at -18V in germanium at two levels of doping

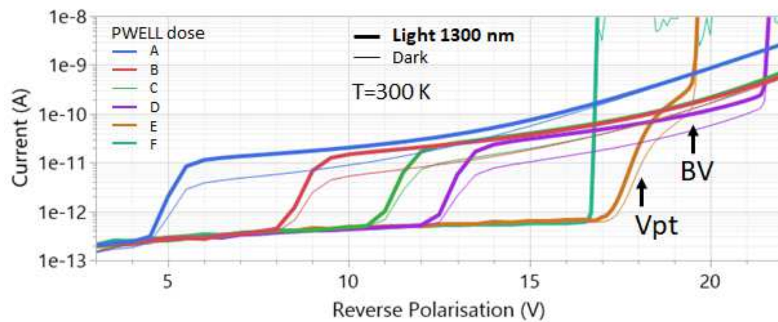

Fig. 4. Current measurement versus bias in dark and under illumination for different PWELL dose.

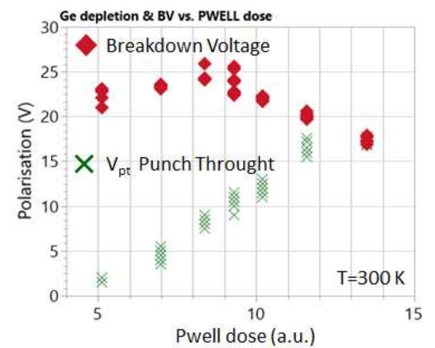

Fig. 5. Measured BV and Vpt versus PWELL dose

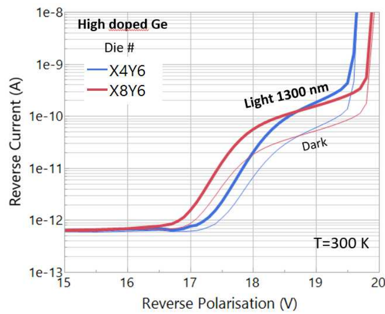

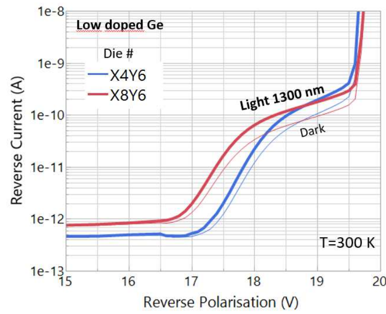

Fig. 6. Dark and light currents on two different SPAD on high doped (left) and low doped (right) germanium wafer

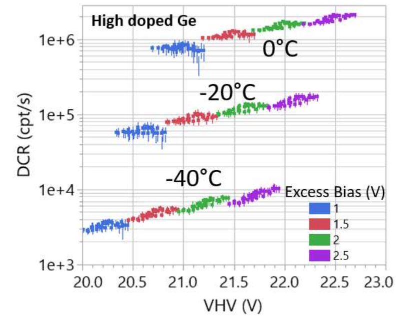

Fig. 7. DCR vs reverse voltage and temperature on high doped germanium wafer

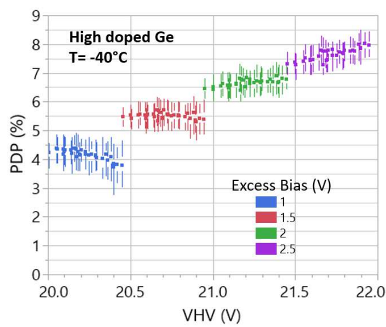

Fig. 8. PDP versus reverse voltage at -40°C

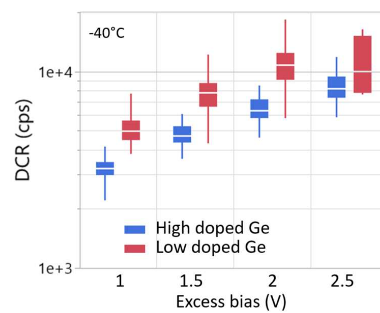

Fig. 9. Comparison of DCR high and low doped germanium (box plot statistics with quantile min., 25%, 50%, 75%, max.)

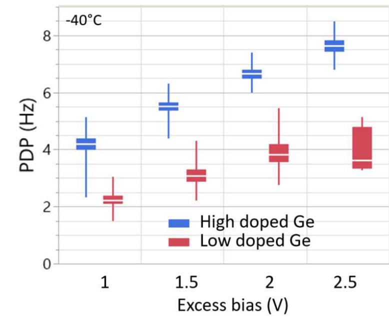

Fig. 10. Comparison of PDP for high and low doped germanium

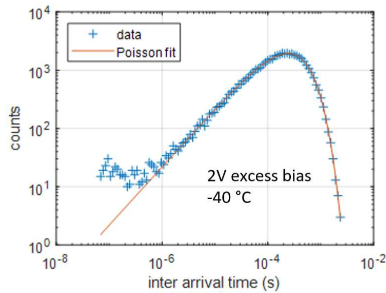

Fig. 11. Histogram of inter-arrival time with Poisson fit at a DCR of 8 kcps

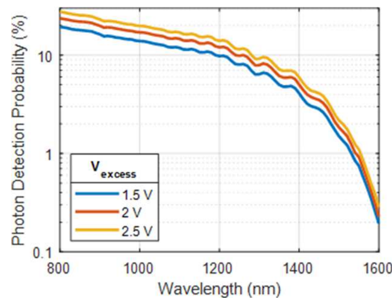

Fig. 12. Sensitivity (PDP) versus wavelength

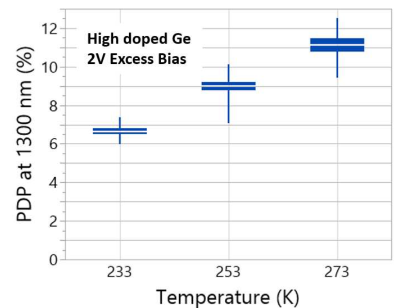

Fig. 13. Evolution of PDP with temperature of the full statistic high Ge doped wafer

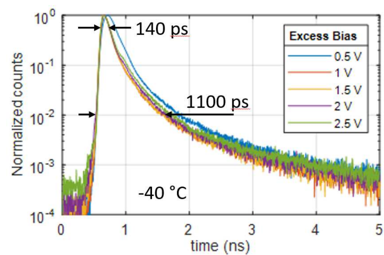

Fig. 14. Jitter measurements at 1300 nm on a SPAD at different excess voltage

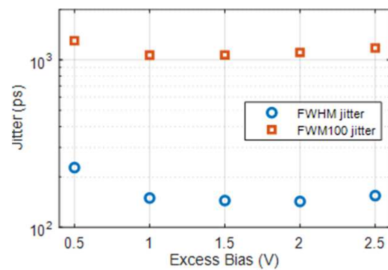

Fig. 15. Jitter at 1310 nm, FWHM and FWHM100 versus Excess bias

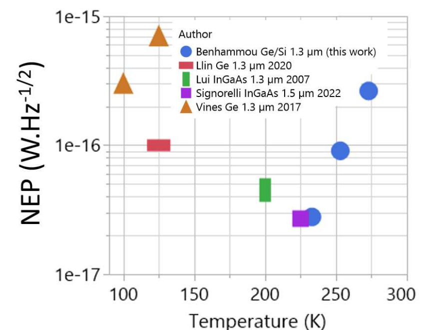

Fig. 16. Noise equivalent power for Ge and InGaAs publications